nature nanotechnology

LETTERS

PUBLISHED ONLINE: 3 AUGUST 2015 | DOI: 10.1038/NNANO.2015.158

Molecular valves for controlling gas phase transport made from discrete ångström-sized pores in graphene

Luda Wang[1†], Lee W. Drahushuk[2], Lauren Cantley[3], Steven P. Koenig[4,5], Xinghui Liu[1], John Pellegrino[1], Michael S. Strano[2] and J. Scott Bunch[3,6*]

An ability to precisely regulate the quantity and location of molecular flux is of value in applications such as nanoscale three-dimensional printing, catalysis and sensor design[1–4]. Barrier materials containing pores with molecular dimensions have previously been used to manipulate molecular compositions in the gas phase, but have so far been unable to offer controlled gas transport through individual pores[5–18]. Here, we show that gas flux through discrete ångström-sized pores in monolayer graphene can be detected and then controlled using nanometre-sized gold clusters, which are formed on the surface of the graphene and can migrate and partially block a pore. In samples without gold clusters, we observe stochastic switching of the magnitude of the gas permeance, which we attribute to molecular rearrangements of the pore. Our molecular valves could be used, for example, to develop unique approaches to molecular synthesis that are based on the controllable switching of a molecular gas flux, reminiscent of ion channels in biological cell membranes and solid-state nanopores[19].

We studied two types of ångström pore molecular valve: a porous single layer of suspended graphene with no gold nanoclusters on its surface (PSLG) and a porous single layer of suspended graphene on top of which we evaporated gold nanoclusters (PSLG–AuNCs). The fabrication of both types of device begins with suspended pristine monolayer graphene, which is impermeable to all gases[20] and is defect-free[21]. The graphene is mechanically exfoliated over predefined etched wells in a silicon substrate with 90 nm of thermal silicon oxide on top. This forms a graphene-sealed microcavity that confines an approximately μm^3 volume of gas underneath the suspended graphene. Two techniques were used to introduce molecular-sized pores. The first uses a voltage pulse applied by a metallized atomic force microscope (AFM) tip[22], while the second introduces a molecular-sized pore at a random spot on a H_2-pressurized, graphene-sealed microcavity using ultraviolet-induced oxidation[23,24].

Figure 1a illustrates the first method, in which a ~300-nm-diameter pore is created in the centre of a graphene membrane by applying a voltage pulse of −5 V for 100 ms. A pressurized blister test was used to determine the leak rate out of the graphene-sealed microcavity[23]. The microcavity was filled with pure H_2 or N_2 at 300–400 kPa and the graphene was observed to bulge up due to the pressure difference across it. An example of an unetched pristine sample pressurized with N_2 is shown in Fig. 1b. In this instance, after applying a voltage pulse of −9 V for 2 s to the centre of the membrane, a single pore is created. We found that the voltage and time needed to introduce a pore varied depending on the AFM tip used, thus the difference in sizes between Fig. 1a and c. Immediately after pore formation, the deflection drops and the graphene is flat except for a few wrinkles introduced by the process (Fig. 1c). The AFM image shows no detectable pore, indicating that the pore is smaller than the resolution of the AFM. For the PSLG–AuNCs samples, gold atoms were evaporated onto the graphene. Figure 1d shows the graphene sample in Fig. 1c after gold evaporation and repressurization with N_2 gas. The graphene is bulging up, indicating that the gold clusters have blocked the pore.

In the second poration method a molecular-sized pore is introduced on a H_2-pressurized, graphene-sealed microcavity using ultraviolet-induced oxidation. The deflection of the graphene was monitored using an AFM operating in intermittent contact mode. Figure 1e–g shows the maximum deflection versus time for three graphene sealed microcavities labelled Membrane 1, Membrane 2 and Membrane 3 formed by the same graphene flake covering three wells. After exposing all the membranes to a series of eight etches, Membrane 2 shows a dramatic change in the deflection just after the last etch that is indicative of a rapid leaking of all the H_2 gas inside the microcavity (any counter-transport of air back into the microcavity is much slower). Membrane 1 and Membrane 3 have leak rates that are relatively unchanged, suggesting that they remain unporated and pristine. Thus, we see that the initiation of ångström-sized porosity in graphene flakes by ultraviolet exposure is a sparse and discrete process. The instantaneous change in the permeance from a very slow leak to a very fast leak is strongly indicative of a single pore being formed. It would be highly unusual (although not impossible) for multiple similar-sized pores to be introduced into Membrane 2 at once while the other two membranes from the same graphene flake remained unporated.

In the first few hours after ultraviolet-induced oxidation of a graphene sample with evaporated gold clusters, the gold clusters were observed to migrate and congregate on the surface of the graphene, sometimes blocking the created pore (Fig. 1j,k). In such a blocked PSLG–AuNC device, the leak rate of H_2 gas out of the microcavity is initially slow, and the graphene deflection changes slowly with time (Fig. 1o). A fit to a membrane mechanics model (Supplementary Section 3) is shown as a red line in Fig. 1s. During scanning there is a sudden jump in the deflection and a

[1]Department of Mechanical Engineering, University of Colorado, Boulder, Colorado 80309, USA. [2]Department of Chemical Engineering, Massachusetts Institute of Technology, Cambridge, Massachusetts 02139, USA. [3]Department of Mechanical Engineering, Boston University, Boston, Massachusetts 02215, USA. [4]Department of Physics, National University of Singapore, Singapore 117542, Singapore. [5]National University of Singapore, Center for Advanced 2D Materials and Graphene Research Centre, Singapore 117546, Singapore. [6]Division of Materials Science and Engineering, Boston University, Brookline, Massachusetts 02446, USA. †Present address: Department of Mechanical Engineering, Massachusetts Institute of Technology, Cambridge, Massachusetts 02139, USA. *e-mail: bunch@bu.edu

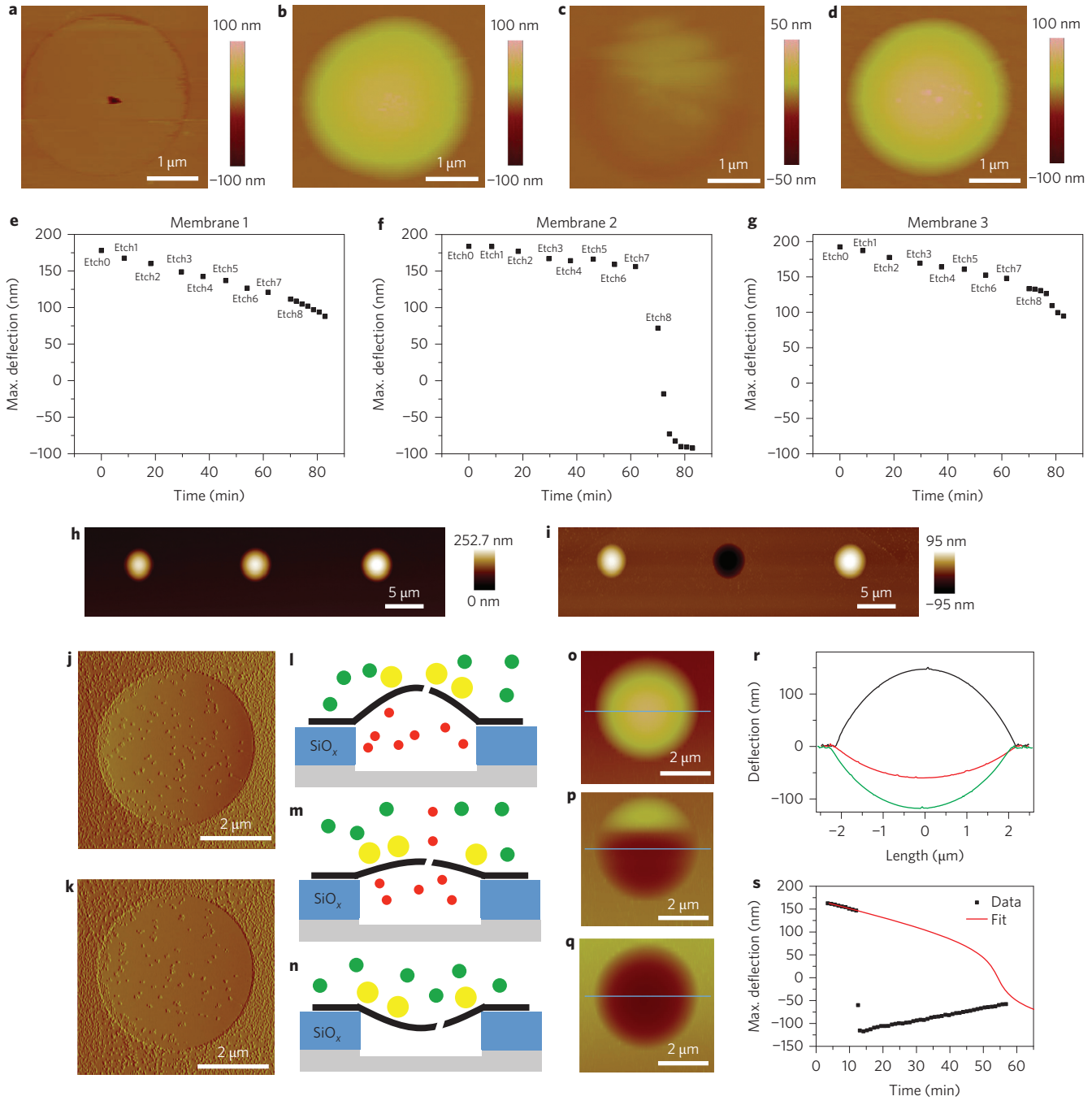

Figure 1 | Fabrication of molecular valves in suspended graphene. a–d, AFM voltage pulse etching to introduce pores into suspended graphene: AFM height image of suspended graphene with a large diameter pore (~300 nm) etched at its centre using AFM voltage pulse etching (**a**); AFM height images of pressurized suspended graphene before (**b**) and ~3 min after (**c**) etching a small pore (~1 nm) at the centre of the membrane using AFM voltage pulse etching (the pore is below the resolution of the AFM and not visible in the image); AFM height image of the same membrane as in **b** and **c**, after gold evaporation and pressurization with N_2 gas (**d**) (the bulged up nature shows that it now holds gas). **e–s**, Ultraviolet etching to introduce pores on suspended graphene: maximum deflection versus time during ultraviolet etching for three graphene sealed microcavities on the same flake (**e–g**) (the ultraviolet etching was stopped after Etch 8); AFM height images corresponding to the first and last points in **e–g** (**h**,**i**); AFM amplitude images showing the movement of gold nanoparticles on suspended graphene (**j**,**k**); schematic of the gold nanoparticles (yellow solid circles) blocking and unblocking the pore on the monolayer graphene (**l–n**); AFM height images capturing the deflection changes illustrated in **l–n** (**o–q**); deflection versus position through the centre of the suspended graphene in **o–q** (**r**); maximum deflection versus time for the dramatic leak rate change (**s**). The solid red line is a fit to the data before switching using a membrane mechanics model.

much faster leak rate is observed (Fig. 1p,q). This change from bulged up to bulged down occurs in ~30 s. A line cut through the centre of the graphene during this process is shown in Fig. 1o. From the line cut (blue lines in Fig. 1o–q), we can see the maximum deflection drops from 147 nm to −115 nm in ~1 min (Fig. 1s). We attribute this sudden change in the deflection to migration of the gold nanoclusters on the surface of the graphene, which 'opened' a single ångström-sized pore in the graphene,

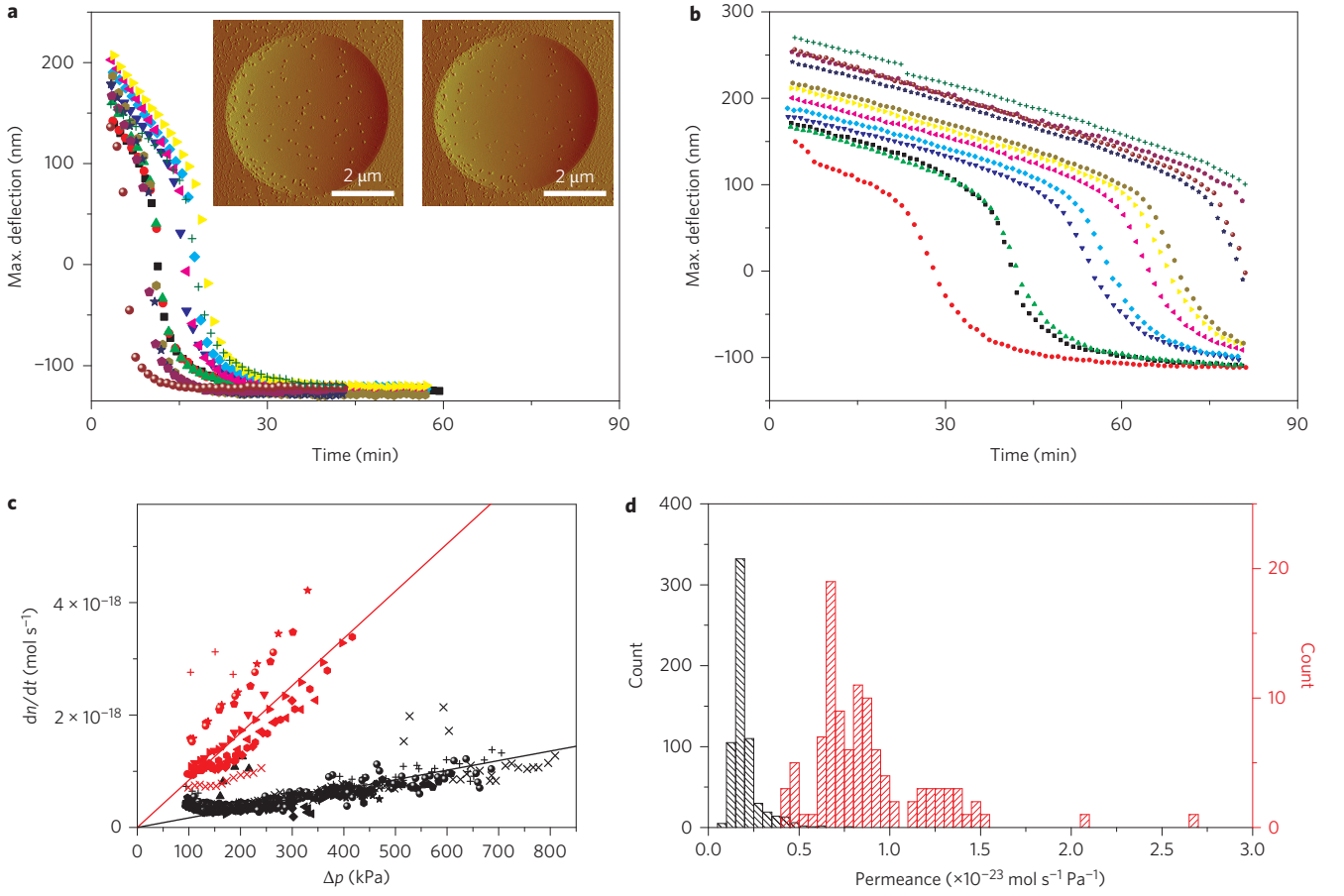

Figure 2 | Controlling the leak rate by laser-induced heating. a,**b**, Maximum deflection of the graphene before (**a**) and after (**b**) focusing a laser beam at the centre of the graphene. Different colours represent different charging pressures. In **a**, the charging pressure sequence is 200 to 700 to 200 kPa, in 100 kPa increments. In **b**, the charging pressure sequence is 200 to 850 kPa, in 50, 100 or 150 kPa increments. Insets in **a**: AFM amplitude images of the suspended graphene corresponding to the state of the graphene deflection for the measurements in **a** (left inset) and **b** (right inset). **c**, Leak rate dn/dt versus pressure difference Δp for **a** (shown in red) and **b** (shown in black). Solid lines are linear fits to the data. **d**, Histogram of the permeance from data in **a** (red) and **b** (black).

allowing a fast leak rate (shown schematically in Fig. 1l–n). As is the case for Membrane 2 in Fig. 1f, a single pore is probably responsible for the sudden change in permeance, as it is unlikely that multiple pores opened simultaneously.

The change in permeance can be trigged by laser-induced heating in vacuum to stimulate movement of the gold nanoclusters (Fig. 2). In such a case, the graphene in Fig. 1 displays a fast permeance, as evidenced by a decrease in the maximum deflection versus time for H_2 gas, taking place in less than 30 min. The permeance is relatively constant over many measurements at different starting internal pressures of hydrogen, suggesting that, eventually, the gold nanoclusters stop migrating. This is further confirmed by AFM images (Fig. 2a inset, left), which show the configuration of nanoclusters to be stable. After shining a laser on the surface of the graphene, the permeance slows considerably, now taking ~30–90 min to leak out depending on the initial internal pressure. Again, the permeance is stable during these measurements over multiple internal pressures. An AFM image of the surface of the graphene after laser exposure shows a change in the configuration of gold nanoclusters on the surface of the graphene (Fig. 2a inset, right).

From the maximum deflection versus time curves in Fig. 2a,b, the rate of change of the number of molecules, n, constitutes a leak rate dn/dt that can be extracted assuming a simple membrane mechanics model (Fig. 2c) (Supplementary Section 2)[23]. We observe that the leak rate shows a linear dependence on the pressure difference with a slope of $8.41 \pm 0.26 \times 10^{-24}$ mol s^{-1} Pa^{-1} before laser exposure and $1.70 \pm 0.02 \times 10^{-24}$ mol s^{-1} Pa^{-1} after laser exposure, consistent with ångström-sized pore transport[25]. A histogram of the leak rate normalized by the pressure difference, which we define as the permeance, is shown in Fig. 2d. Counts on the histogram correspond to a permeance calculation based on the slope around each deflection data point. There are clearly two defined states of the permeance before and after laser exposure. Additional heating with the laser leads to pore opening, showing that this process is repeatable and reversible (Supplementary Section 4), demonstrating the ability to control the gas flux through a single ångström-sized pore molecular valve.

Gas transport through the ångström-sized pore can be modelled using classical effusion. When the pore size is smaller than the mean free path of the molecule, classical effusion dictates that the time constant for the decay of the number of molecules in the graphene sealed microcavity is given by

$$\tau = \frac{V}{\gamma}\sqrt{\frac{2\pi M_w}{RT}} \quad (1)$$

where V is the volume of the container, γ is the transmission coefficient, M_w is the molecular mass, R is the ideal gas constant, and T is the temperature[26]. The transmission coefficient γ incorporates both the physical geometry of the pore and any energy barrier from molecular interactions between the molecule and the pore. Due to the volume of gas in the graphene sealed microcavity (~1 μm^3), the time constant for the effusion due to a single ångström-sized pore

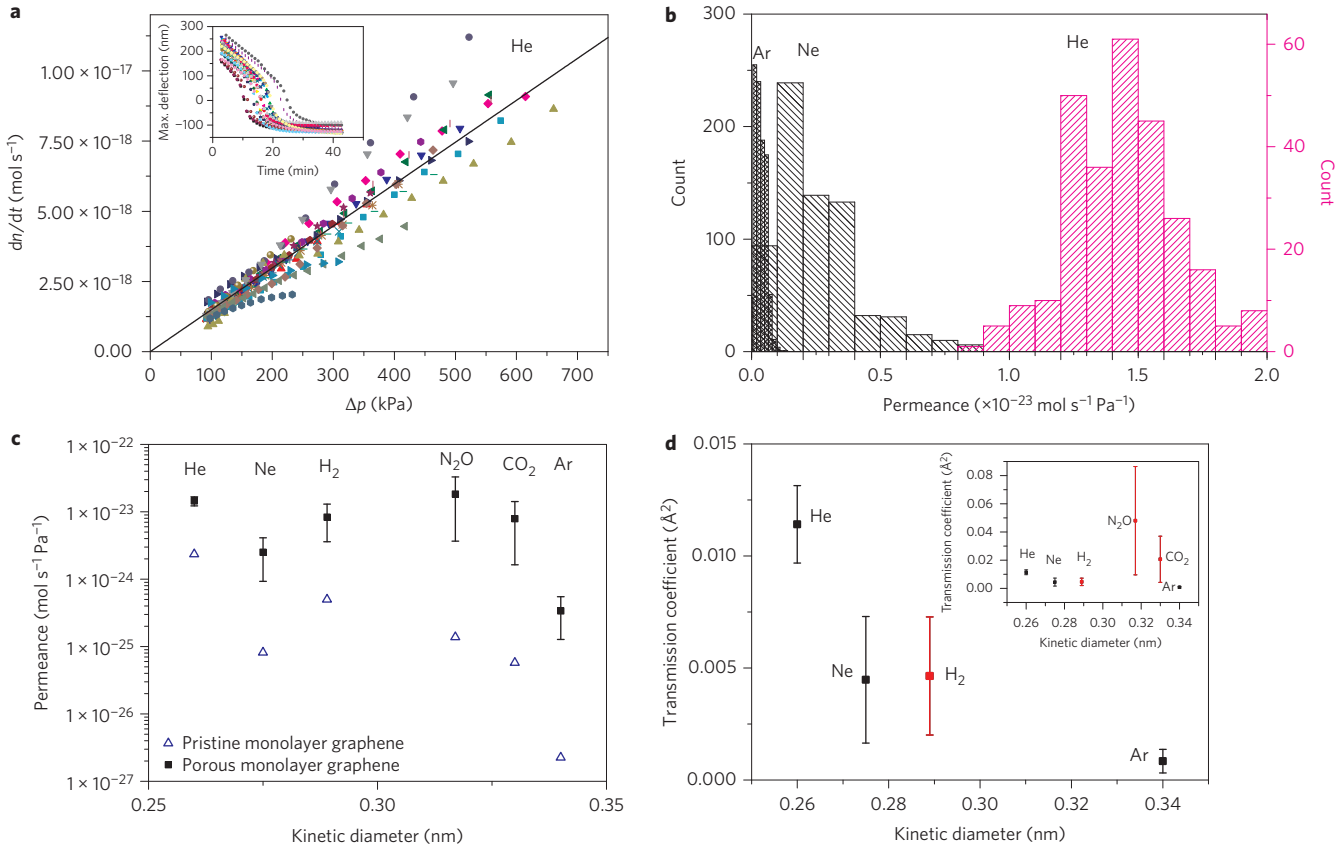

Figure 3 | Leak rates of gases through porous monolayer suspended graphene without gold nanoparticles. a, Leak rate dn/dt versus pressure difference Δp for He gas. Solid line is a linear fit to the data. Inset: maximum deflection versus t for He gas. **b**, Histogram of permeance for Ar, Ne and He. **c**, Permeance versus kinetic diameter for all measured gases before (blue) and after (black) etching. **d**, Transmission coefficient (calculated from equation (2)) versus kinetic diameter for He, Ne, H_2 and Ar. Inset: transmission coefficient (calculated from equation (2)) versus kinetic diameter for He, Ne, H_2, N_2O, CO_2 and Ar. Error bars in **c**,**d** represent ±s.d. for different measurements on the same membrane.

can be minutes, making our geometry ideally suited for measuring the leak rate through a single sub-nanometre pore and for observing sub-Å^2 changes in the transmission coefficient. Correspondingly, the leak rate dn/dt, assuming classical effusion, is given by

$$\frac{\mathrm{d}n}{\mathrm{d}t} = \frac{\gamma}{\sqrt{2\pi M_w RT}} \cdot \Delta p \qquad (2)$$

where Δp is the partial pressure difference across the graphene[25]. A plot of dn/dt versus Δp shows a linear dependence, further supporting classical effusion (Fig. 2c). The transmission coefficient can be deduced from the slope and changes from 0.0047 Å^2 (before) to 0.00095 Å^2 (after) laser heating. The transmission coefficient is the geometric area of the pore (a few Å^2) multiplied by a transmission probability that an impinging gas atom or molecule has sufficient energy to pass through the potential barrier of the pore. Hence, γ is considerably smaller than the cross-sectional area of the test gas H_2 (2.89 Å), providing evidence that the pore is on the order of the kinetic diameter of H_2 and we are measuring small changes in the energy barrier from molecular interactions between the gas and pore mouth.

The ability to observe small changes in γ allows us to vary the molecular size and study how that influences gas transport in the same PSLG. In this study we used a single PSLG that contained no gold nanoclusters, and four additional etching exposures were carried out after the first observed rapid change in deflection (indicating the formation of a pore). The leak rate dn/dt of He gas through the PSLG shows a linear dependence on Δp and is relatively constant over a range of Δp from ~100 kPa to 700 kPa (Fig. 3a, inset). This agrees with classical effusion with a slope equal to $1.5 \pm 0.01 \times 10^{-23}$ mol s^{-1} Pa^{-1}, corresponding to $\gamma = 0.011$ Å^2 (Fig. 3a). The permeance for the noble gases, Ar, Ne and He, are shown as a histogram, with average values and standard deviations of 3.4 ± 2.1, 25 ± 16 and $150 \pm 20 \times 10^{-25}$ mol s^{-1} Pa^{-1}, respectively. This follows a trend of a lower permeance for larger gas atoms. In addition to the noble gases, we measured the permeance of the non-noble gas molecules H_2, CO_2 and N_2O, both before and after introducing the molecular-sized pore (Fig. 3c). Data for the non-porated graphene (Supplementary Section 1) were taken on four separate but similar monolayer graphene membranes, and the measured leak rates agree well with a leak primarily through the underlying silicon oxide substrate[20,23,27]. In all cases there was a considerable increase in the leak rate after poration, supporting the conclusion that the leak rate is primarily permeation through the molecular-sized pore.

Using equation (2) we can deduce the transmission coefficient as a function of the kinetic diameter for all the gases measured. As expected for the noble gases, the transmission coefficient increases as the kinetic diameter decreases—(Ar) 0.00084 ± 0.00053 Å^2, (Ne) 0.0045 ± 0.0028 Å^2 and (He) 0.011 ± 0.002 Å^2 (Fig. 3d)—further confirming that the pore size is on the order of the kinetic diameter and showing the influence of the molecular size on γ. In addition, the leak rate of H_2 roughly follows the trend observed with the noble gas atoms. However, CO_2 and N_2O follow a very different trend (inset Fig. 3d). Their transmission coefficients are considerably larger than one would expect from their kinetic

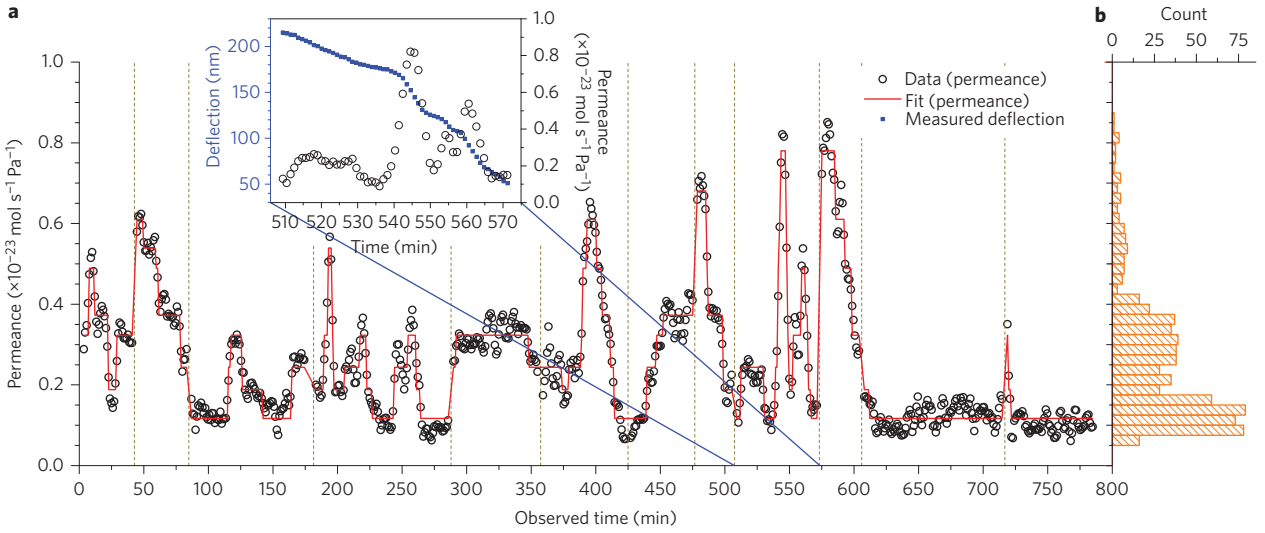

Figure 4 | Stochastic switching of the leak rate through porous monolayer graphene without gold nanoparticles. a, Permeance (black circles) and fit (red line) versus time for all Ne data. Bottom axis: observed time, corresponding to the 800 min of measurements taken over five days after repeated pressurization. Each measurement is separated by a vertical dashed line. Inset: Single experimental run for the highlighted time range. Left axis: maximum deflection versus time for Ne (blue squares). Right axis: permeance versus time calculated from the change in deflection versus time (black circles). **b**, Histogram of the permeance (on the vertical axis of **a**) for all the data in **a**.

diameter—(CO_2) 0.021 ± 0.016 Å^2 and (N_2O) 0.048 ± 0.038 Å^2. We attribute this to the chemical interactions that N_2O and CO_2 have with the pore, which lower the energy barrier for transport. These experiments demonstrate that the gas transport of gas molecules with polar bonds clearly shows a strong influence on chemical interactions between the molecule and the pore, consistent with recent theoretical calculations[28,29].

Although the permeances are nominally constant over long time periods (days) of measurements, the transmission coefficient demonstrates discretized fluctuations indicative of stochastic switching. Figure 4a illustrates the concatenated permeances of Ne over time along with a fit to discrete states using hidden Markov modelling (HMM; Supplementary Section 7). The data in Fig. 4a were taken over the course of five days. Vertical dashed lines correspond to the start of a new measurement. All measurements are concatenated into a single observed time axis so that the repetition of certain states and values of permeance can be seen. This switching is clearly seen in the inset of Fig. 4a, where the permeance switches five times within 1 h (black circles). The histogram of the permeance for Ne is plotted in Fig. 4b. The permeance shows a large number of states on the low end of the spectrum with occasional switching to faster leak rates. We fit these permeance values versus time to discrete states and applied an HMM to elucidate transition rates[30,31]. Additional analysis was applied to show that the numerous observed states are consistent with a system having three independent pores with two states each. The frequency of switching between the states, averaged across three pores, yields an approximate value for the activation energy of the switching process (1 eV) with three two-state pores (Supplementary Section 8). This is comparable to the activation energy required for the rearrangement of molecular bonds, such as *cis–trans* isomerization[32]. These calculations using our experimental results demonstrate that relatively minor changes in a pore's configuration can have an observable impact on its permeation characteristics.

In conclusion, we have demonstrated a type of molecular valve in graphene that allows us to control the gas flux through discrete ångström-sized pore. The process was controlled by movement of gold nanoclusters on the graphene surface. These results lead to a greater mechanistic understanding of molecular gas transport through molecular-sized pores in atomically thin materials. The switching observed may lead to unique sensors based on the reversible switching of molecular transport through approximately ångström-sized pores, reminiscent of ion channels in biological cell membranes.

Methods

Methods and any associated references are available in the online version of the paper.

Received 24 April 2014; accepted 19 June 2015;
published online 3 August 2015

References

1. Piner, R. D., Zhu, J., Xu, F., Hong, S. H. & Mirkin, C. A. 'Dip-pen' nanolithography. *Science* **283,** 661–663 (1999).
2. Albrecht, P. M., Barraza-Lopez, S. & Lyding, J. W. Preferential orientation of a chiral semiconducting carbon nanotube on the locally depassivated Si(100)–2×1:H surface identified by scanning tunneling microscopy. *Small* **3,** 1402–1406 (2007).
3. Chen, P. *et al.* Spatiotemporal catalytic dynamics within single nanocatalysts revealed by single-molecule microscopy. *Chem. Soc. Rev.* **43,** 1107–1117 (2014).
4. Imboden, M. *et al.* Building a fab on a chip. *Nanoscale* **6,** 5049–5062 (2014).
5. Park, H. B. *et al.* Polymers with cavities tuned for fast selective transport of small molecules and ions. *Science* **318,** 254–258 (2007).
6. Strathmann, H. Membrane separation processes: current relevance and future opportunities. *AIChE J.* **47,** 1077–1087 (2001).
7. Lai, Z. P. *et al.* Microstructural optimization of a zeolite membrane for organic vapor separation. *Science* **300,** 456–460 (2003).
8. Shiflett, M. B. & Foley, H. C. Ultrasonic deposition of high-selectivity nanoporous carbon membranes. *Science* **285,** 1902–1905 (1999).
9. Hinds, B. J. *et al.* Aligned multiwalled carbon nanotube membranes. *Science* **303,** 62–65 (2004).
10. Ahn, J. Y., Chung, W. J., Pinnau, I. & Guiver, M. D. Poly sulfone/silica nanoparticle mixed-matrix membranes for gas separation. *J. Membrane Sci.* **314,** 123–133 (2008).
11. de Vos, R. M. & Verweij, H. High-selectivity, high-flux silica membranes for gas separation. *Science* **279,** 1710–1711 (1998).
12. Jiang, D. E., Cooper, V. R. & Dai, S. Porous graphene as the ultimate membrane for gas separation. *Nano Lett.* **9,** 4019–4024 (2009).
13. Kim, H. W. *et al.* Selective gas transport through few-layered graphene and graphene oxide membranes. *Science* **342,** 91–95 (2013).
14. Li, H. *et al.* Ultrathin, molecular-sieving graphene oxide membranes for selective hydrogen separation. *Science* **342,** 95–98 (2013).
15. Boutilier, M. S. H. *et al.* Implications of permeation through intrinsic defects in graphene on the design of defect-tolerant membranes for gas separation. *ACS Nano* **8,** 841–849 (2014).

16. Joshi, R. K. *et al.* Precise and ultrafast molecular sieving through graphene oxide membranes. *Science* **343,** 752–754 (2014).
17. Drahushuk, L. W. & Strano, M. S. Mechanisms of gas permeation through single layer graphene membranes. *Langmuir* **28,** 16671–16678 (2012).
18. Nair, R. R., Wu, H. A., Jayaram, P. N., Grigorieva, I. V. & Geim, A. K. Unimpeded permeation of water through helium-leak-tight graphene-based membranes. *Science* **335,** 442–444 (2012).
19. Dekker, C. Solid-state nanopores. *Nature Nanotech.* **2,** 209–215 (2007).
20. Bunch, J. S. *et al.* Impermeable atomic membranes from graphene sheets. *Nano Lett.* **8,** 2458–2462 (2008).
21. Hu, S. *et al.* Proton transport through one-atom-thick crystals. *Nature* **516,** 227–230 (2014).
22. Park, J. Y., Yaish, Y., Brink, M., Rosenblatt, S. & McEuen, P. L. Electrical cutting and nicking of carbon nanotubes using an atomic force microscope. *Appl. Phys. Lett.* **80,** 4446–4448 (2002).
23. Koenig, S. P., Wang, L. D., Pellegrino, J. & Bunch, J. S. Selective molecular sieving through porous graphene. *Nature Nanotech.* **7,** 728–732 (2012).
24. Ozeki, S., Ito, T., Uozumi, K. & Nishio, I. Scanning tunneling microscopy of UV-induced gasification reaction on highly oriented pyrolytic graphite. *Jpn. J. Appl. Phys.* **35,** 3772–3774 (1996).
25. Sun, C. *et al.* Mechanisms of molecular permeation through nanoporous graphene membranes. *Langmuir* **30,** 675–682 (2013).
26. Reif, F. *Fundamentals of Statistical and Thermal Physics* (McGraw-Hill, 1965).
27. Koenig, S. P., Boddeti, N. G., Dunn, M. L. & Bunch, J. S. Ultrastrong adhesion of graphene membranes. *Nature Nanotech.* **6,** 543–546 (2011).
28. Liu, H., Dai, S. & Jiang, D.-E. Insights into CO_2/N_2 separation through nanoporous graphene from molecular dynamics. *Nanoscale* **5,** 9984–9987 (2013).
29. Shan, M. *et al.* Influence of chemical functionalization on the CO_2/N_2 separation performance of porous graphene membranes. *Nanoscale* **4,** 5477–5482 (2012).
30. Jin, H., Heller, D. A., Kim, J. H. & Strano, M. S. Stochastic analysis of stepwise fluorescence quenching reactions on single-walled carbon nanotubes: single molecule sensors. *Nano Lett.* **8,** 4299–4304 (2008).
31. McKinney, S. A., Joo, C. & Ha, T. Analysis of single-molecule FRET trajectories using hidden Markov modeling. *Biophys. J.* **91,** 1941–1951 (2006).
32. Cembran, A., Bernardi, F., Garavelli, M., Gagliardi, L. & Orlandi, G. On the mechanism of the *cis–trans* isomerization in the lowest electronic states of azobenzene: S_0, S_1, and T_1. *J. Am. Chem. Soc.* **126,** 3234–3243 (2004).

Acknowledgements

The authors thank X. Yin for useful discussions and A. Swan, B. Goldberg and J. Christopher for assistance with Raman spectroscopy. This work was supported by the National Science Foundation (NSF), grant no. 1054406 (CMMI: CAREER, Atomic Scale Defect Engineering in Graphene Membranes), the NSF Industry/University Cooperative Research Center for Membrane Science, Engineering and Technology (MAST), in part by the National Nanotechnology Infrastructure Network (NNIN) and the NSF under grant no. ECS-0335765 and the NSF Graduate Research Fellowship under grant no. DGE-1247312. The theory and modelling part was supported (in part) by the US Army Research Office under contract no. W911NF-13-D-0001.

Author contributions

L.W., L.C. and S.P.K. performed the experiments. L.W. and J.S.B. conceived and designed the experiments. L.W.D. and M.S.S. developed the theory and modelling. L.W., L.C., S.P.K. and X.L. prepared and fabricated the samples. L.W., L.W.D., J.P., M.S.S. and J.S.B. interpreted the results and co-wrote the manuscript.

Additional information

Supplementary information is available in the online version of the paper. Reprints and permissions information is available online at www.nature.com/reprints. Correspondence and requests for materials should be addressed to J.S.B.

Competing financial interests

The authors declare no competing financial interests.

Methods

The device fabrication and pressurization techniques closely follow refs 20, 23, 27 and 33. Suspended graphene was fabricated using mechanical exfoliation on silicon oxide substrates with predefined etched wells. The wells were defined by photolithography on an oxidized silicon wafer with 90 nm silicon oxide on top and had a diameter of ~3–5 μm. Reactive ion etching was used to etch the wells to a depth of ~400–1,000 nm, and the 'scotch tape' method was used to deposit graphene over the wells. Gold atoms were evaporated onto the graphene in vacuum (CVC 3-boat thermal evaporator, at 0.1 Å s^{-1} for less than 0.5 s). For some devices we evaporated gold atoms before poration and for others we evaporated gold atoms after poration. No significant difference between these was found.

To pressurize the inside of the microcavity we placed the sample into a high-pressure chamber with a particular gas species at a prescribed pressure (the 'charging pressure'). After several hours or days, depending on the gas species used, the pressure in the microcavity comes into equilibrium with the charging pressure. The pristine graphene sheet is impermeable to any gases, but the gas can diffuse through the silicon oxide substrate. The period required to reach ambient pressure equilibrium ranges from ~4 to 30 days, depending on the gas species.

After measuring the leak rate for the pristine graphene, pores were etched by exposing the graphene to an ultraviolet lamp ($\lambda_1 = 185$ nm, $\lambda_2 = 254$ nm) under ambient conditions. The microcavities were first pressurized with pure H_2 up to 200 kPa above ambient pressure. Once the microcavity reached equilibrium it was removed from the pressure chamber, and the deflection was measured by AFM. This was followed by a series of short ultraviolet exposures then AFM scans. Once a pore was created with a size between the dimensions of H_2 and N_2, the deflection abruptly changed from positive to negative. After creation of a pore, the leak rate was dominated by transport through the pores, and ~1–12 h of pressurization, depending on the gas species, was sufficient for equilibration.

To create pores by the voltage pulse method we first pressurized the graphene with N_2 to 300 kPa above ambient pressure. A triggered force curve was then applied under ambient conditions using a metallized AFM tip. The bias voltage was applied while the tip was in contact with the surface of the graphene membrane. This was repeated with an increasing magnitude of voltage and contact time until a pore was created. The pore was detected by observing an abrupt decrease in deflection.

Laser heating of the suspended graphene was accomplished using a He–Ne laser or a solid-state laser ($\lambda = 633$ or 532 nm) with a power of ~1–10 mW, as measured before it entered the vacuum chamber through a sapphire window. The laser spot size was estimated to be 3.5 μm with an exposure time of 5 min.

References

33. Wang, L. D. *et al.* Ultrathin oxide films by atomic layer deposition on graphene. *Nano Lett.* **12,** 3706–3710 (2012).